Different Doping Behaviour of Silicon in Zinc Blende and Wurtzite GaAs Nanowires: Implications for Crystal-Phase Device Design

Qichao Hou,[ak] H. Aruni Fonseka,[b] Faustino Martelli,[c] Barbara Paci,[d] Anders Gustafsson,[f] James A. Gott,[b] Hui Yang,[*g] Suguo Huo,[h] Xuezhe Yu,[e] Lulu Chen,[a] Yanmeng Chu,[a] Chaofei Zha,[ai] Zheyu Zhang,[a] Linjun Zhang,[a] Fuxiang Shang,[a] Wenzhang Fang,[jk] Zhiyuan Cheng,[ak] Ana M. Sanchez,[b] Huiyun Liu,[e] Yunyan Zhang,[*aek]

[a.] *School of Micro-Nano Electronics, Zhejiang University, Hangzhou, Zhejiang, 311200, China*

[b.] *Department of Physics, University of Warwick, Coventry CV4 7AL, United Kingdom*

[c.] *Istituto per la Microelettronica e i Microsistemi, IMM-CNR, via fosso del cavaliere 100, 00133 Roma, Italy*

[d.] *Istituto di Struttura della Materia, ISM-CNR, via fosso del cavaliere 100, 00133 Roma, Italy*

[e.] *Department of Electronic and Electrical Engineering, University College London, London WC1E 7JE, United Kingdom*

[f.] *Solid State Physics and NanoLund, Lund University, Box 118, SE-221 00 Lund, Sweden*

[g.] *Department of Materials, Imperial College London, Exhibition Road, London SW7 2AZ, United Kingdom*

[h.] *London Centre for Nanotechnology, University College London, WC1H 0AH, United Kingdom*

[i.] *State Key Laboratory of Information Photonics and Optical Communications, Beijing University of Posts and Telecommunications, Beijing, 100876, China*

[j.] *Department of Polymer Science and Engineering, Zhejiang University, Hangzhou, Zhejiang, 310013, China.*

[k.] *ZJU-Hangzhou Global Scientific and Technological Innovation Center, Hangzhou, Zhejiang, 311200, China.*

Abstract:

The crystal-phase engineering between zinc blende (ZB) and wurtzite (WZ) structures is becoming an important method in designing unique optoelectronic and electronic semiconductor devices. Doping to engineer their electric properties is thus of critical importance, but a direct experimental comparison in doping these two crystal structures is still missing. Nanowires (NWs) allow the coexistence of both structures due to their special growth mode. The differences in dopant incorporation between the two phases are studied here in GaAs NW shells that are coherently grown around the NWs, hence maintaining the crystal structure of the core. The Si dopant is observed to have a higher incorporation efficiency into the WZ

structure due to a 2-times lower incorporation energy compared with that of ZB structure. Besides, it can also be predicted that the Si is more inclined towards Ga-sites in both structures. Indeed, the As-site doping energy of the WZ structure is several orders of magnitude higher than that of Ga-sites, allowing a lower doping compensation effect. This work provides useful information for doping control and hence designing crystal-phase devices.

Key words: Si doping, zinc blende structure, wurtzite structure, nanowire, doping efficiency, crystal-phase devices

Introduction

Nanowires (NWs) have unique mechanical, optical and electronic characteristics that are not observed in thin films.[1-5] They can make semiconductor materials stable in both zinc blende (ZB) and wurtzite (WZ) structures, which is in contrast to most bulk structures like III-Vs that only exist one of the phases. It has been demonstrated that both ZB and WZ can be grown into the same NW,[6] and the layer thickness can be controlled to atomic level, forming crystal-phase superlattices.[7] The possibility to engineer crystal phases can provide an important method in designing unique optoelectronic and electronic semiconductor devices with the rapid development of nanoscience.[8] Depending on the material, changing the crystal phase can switch the indirect-bandgap material, such as GaP and Ge, into direct-bandgap, greatly enhancing the light emission.[9-11]The coexistence of the two structures in a NW can lead to charge confinement, such as quantum dots[12] and superlattices[7].

For a vast majority of semiconductor devices, the construction requires the incorporation of impurities as dopants to tune the electrical properties of different parts of the devices, such as the p-i-n junctions in light emitters and photovoltaics, the p-n junction in a bipolar transistor, and the source/drain in field-effect transistors.[13-18] Besides, doping is also an effective method to improve the performance of nano-devices. For example, controlled doping can significantly increase the photoconductivity lifetime of GaAs NWs by over one order of magnitude, and thus it can be used to reduce the effects of parasitic surface recombination in optoelectronic NW devices.[19,20] The doping can also effectively reduce the depletion region width of NWs and reduce the negative impacts caused by the surface states.[21,22] Thus, the understanding and controlling of the doping behaviours of NWs are essential.

There are many reports on the study of this topic, including the doping paths, concentration limits, sites, etc.[21-33] However, to our knowledge, there is little research on the doping-behaviour differences between the ZB and WZ phases of NWs.[34-36] Especially, the direct experimental comparison is missing which could be due to the challenging measurements on the two crystal phases grown under similar conditions. The coexistence of both ZB and WZ crystal phases in the same NW can be achieved using core-shell structured NWs. The shells grown on these core

NWs follow the crystal template of the former one, and both ZB and WZ crystal phases can exist simultaneously in the same NW, which provides a possibility for studying the differences in doping behavior between two crystal phases under extremely similar growth environments.

In this study, the doping behaviour difference of WZ and ZB crystal phases is studied using the shells of GaAs core-shell NWs. The doping efficiency difference between the two phases has been observed experimentally by Micro-Raman measurements and the incorporation site preference is also predicted theoretically, providing useful information for guiding the understanding and control of the crystal-phase doping.

Experimental section

NW growth: The self-catalyzed GaAs NWs were grown directly on *p*-type Si substrates by means of solid-source III-V molecular beam epitaxy (MBE).[37] GaAs NWs were grown with a Ga beam equivalent pressure, V/III flux ratio, substrate temperature, and growth duration of 7.16×10^{-8} Torr, 40, ~630°C, and 1 hour, respectively. The GaAs shell was grown with a Ga beam equivalent pressure, V/III flux ratio, substrate temperature, and growth duration of 7.16×10^{-8} Torr, 50, ~550 °C, and 1 hour, respectively. Si dopants were introduced during the shell growth. For the GaAsP/GaAs quantum well NWs, the core GaAsP NW was grown with a Ga beam equivalent pressure, V/III flux ratio, P/(As + P) flux ratio, substrate temperature, and growth duration of 8.41×10^{-8} Torr, ~40, 25%, ~640 °C, and 1.5 h, respectively. Two GaAsP shells were then grown with a Ga beam equivalent pressure, V/III flux ratio, P/(As + P) flux ratio, substrate temperature, and growth duration of 8.41×10^{-8} Torr, 50, 50%, ~550 °C, and 30 min, respectively. A ~10 nm GaAs QW was grown between the two GaAsP shells, with a Ga beam equivalent pressure, V/III flux ratio, substrate temperature, and growth duration of 8.41×10^{-8} Torr, 60, ~550 °C, and 10 min, respectively. During growth, the substrate temperature was measured by a pyrometer. The growth process diagram, and structural schematic diagram of Si-doped/undoped GaAs core-shell NWs are shown in Figure 1.

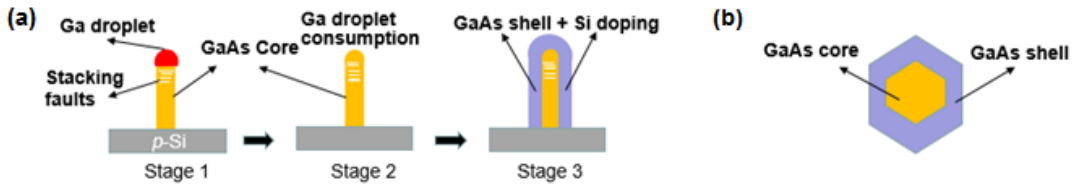

Figure 1. (a) Growth process diagram, and (b) structural schematic diagram of Si-doped/ undoped GaAs core-shell NWs.

Density functional theory modelling: The starting points for our calculations were the experimentally determined structures of ZB GaAs[38] and theoretical WZ GaAs. In both supercell include 4 Ga and 4 As atoms.

Theoretical calculations were performed using plane-wave pseudopotential density functional theory (DFT) formalism implemented in Vienna Ab-initio Simulation Package (VASP).[39] For relaxation calculations, we have used the scalar relativistic all-electron Blöchl's projector augmented-wave (PAW) method.[40-42] Perdew-Burke-Ernzerhof (PBE) functional[43] was used alongside dispersion correction of the Grimme's method (DFT-D3).[44]

Γ-centered Monkhorst-Pack k-point meshes are 3×3×3 and 3×5×3 for ZB and WZ, respectively. The energy cutoff for the plane-wave basis set was set to 600 eV. During the geometric optimization, the total energy was converged to within 1 meV per atom, and a force tolerance of 0.001 eV/Å was set for convergence of the ion positions to ensure accurate atomic positions and lattice parameters.

Here are the optimization structure parameters, zinc blende GaAs (a=5.658) and wurtzite GaAs (a=b=3.985, c=6.563, alpha=90, beta=90, gamma=120). We have adopted one Si for either Ga or As atoms. The formation energy of a substitutional defect that a Si atom replace a Ga or As atom in a GaAs supercell is calculated as follows $ED = E_{(\text{supercell with defect})} + \mu_{(Ga/As)} - \mu_{(Si)} - E_{(\text{defect-free supercell})}$

Where $E_{(\text{supercell with defect})}$ is the energy of the supercell with a given defect, $E_{(\text{defect-free supercell})}$ is the energy the perfect supercell, $\mu_{(Si)}$ is the chemical potential of Si and $\mu_{(Ga/As)}$ is the chemical potential of Ga or As.

Scanning electron microscope (SEM): The NW morphology was measured using Zeiss XB 1540 FIB/SEM and Zeiss Gemini 500 SEM systems.

Transmission electron microscopy (TEM)*:* Simple mechanical transfer of the NWs onto lacey carbon support grids was used to prepare TEM specimens. The STEM and TEM measurements were performed using doubly-corrected ARM200F and Jeol 2100 microscopes, operating at 200 kV. Energy Dispersive X-Ray Spectroscopy (EDX) measurements were performed using an Oxford instruments 100 mm^2 windowless detector installed within the ARM200F microscope.

Cathodoluminescence (CL): CL mapping was acquired using a Gatan MonoCL3 spectrometer at 85 K. CL spectra were acquired using a spectral resolution of 5 nm. Additional 8K CL data was recorded using a Delmic Sparc system for hyperspectral and monochromatic imaging.

Raman measurement: Micro-Raman measurements were performed on as grown samples and on single NWs after their mechanical transfer on a quartz substrate. An InVia Renishaw system equipped with a 100X (NA=0.85) objective and a 457 nm laser has been used. The focused laser spot had a diameter of about 600 nm. The excitation intensity (~ 9 mW/cm^2) has been carefully chosen to avoid any heating of the NWs.

Results and discussion

Un-doped GaAs core NWs were first grown by molecular beam epitaxy (MBE) via self-catalysed mode on Si substrates.[45,46] The majority of NWs are standing vertically on the substrate as can be seen in the scanning electron microscope (SEM) image in Figure 2a. They have a uniform diameter of ~60 nm as seen in the transmission electron microscopy (TEM) image in Figure 2b. On tip of each NW, there is a round Ga droplet, which confirms the self-catalyzed growth mode. The tip (about 1 µm in length) of the NWs has high-density of stacking faults, containing twins, WZ segments, and a mixture of both crystal phases, as can be seen by the dark stripes across the NW diameter shown in Figure 2b. Figure 2c corresponds to a higher magnification image of the tip, which further revealing the twinning and poly-type structure in

this area that can be confirmed by the electron diffraction pattern (inset in Figure 2c). In contrast, the rest part of the NWs has a pure ZB crystal structure with occasional single twins (Indicated with purple arrows in Figure 2b).

After the core NW growth, the droplet was consumed, and then a layer of GaAs shell was grown with a nominal thickness of 60 nm. As a comparison, two samples were prepared, one un-doped and another with a nominal Si doping concentration of 2×10^{19} cm^{-3}. Both the un-doped and doped NWs (Figure 2d and e, respectively) have quite similar morphologies and no doping induced changes are observed (Figure 2f-g). The NWs have a diameter ~200 nm and the sidewalls are quite smooth (Figure 2h). The tip part of the both core-shell structures has a high-density of stacking faults, consistent with the core NWs. The topmost part of NW is commonly enlarged with an irregular shape, which is caused by the un-optimized consumption of the Ga catalytic droplet after the core-NW growth (Figure 2i).

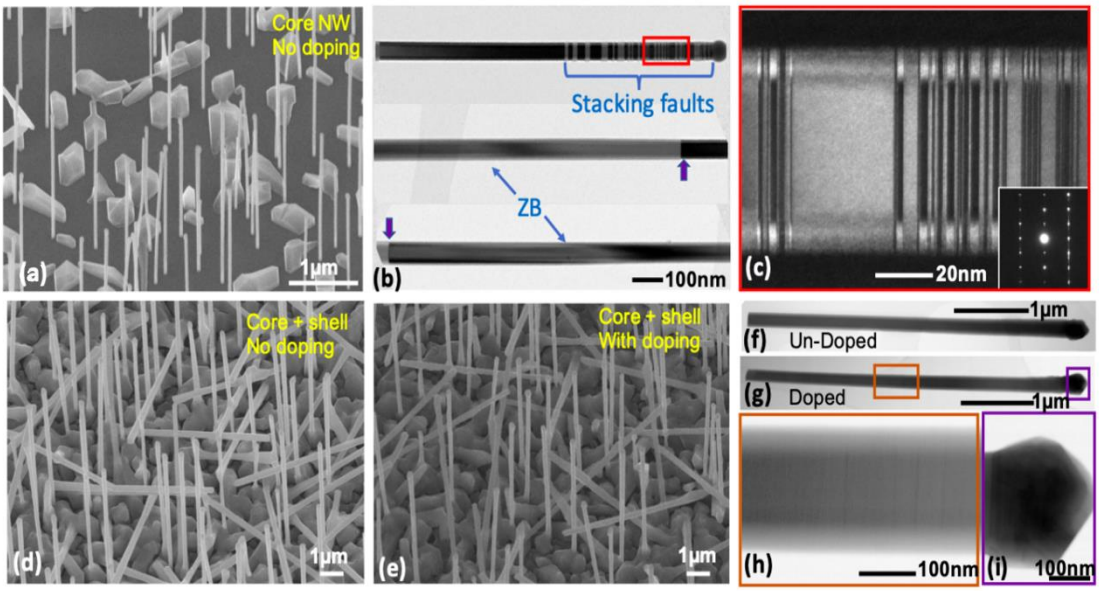

Figure 2. GaAs core-shell NWs with and without doping. (a) Un-doped core NWs. (b) Low-magnification TEM image of a NW from (a). (c) Higher-magnification TEM image of an area

close to the NW tip marked by the red square in (b). The inset is the electron diffraction pattern from the segment. NWs with a (d) un-doped shell and (e) doped shell with a nominal concentration of 2×10^{19} cm^{-3}. Low-magnification TEM images of (f) un-doped and (g) doped NWs from (d) and (e), respectively. (h) and (i) are the high-magnification TEM images of segments marked by red and purple squares in (g), respectively.

The emission properties of the doped NWs were characterized by cathodoluminescence (CL). NW shows a sharp single peak at ~840 nm at 85 K (Figure 3a). The CL mapping in Figure 3b revealed an uneven emission distribution, and the short segment close to one end of the NWs commonly shows much stronger emission. As can be seen clearly in Figure 3c, the strong emission segment is about 1 μm in length and located at the upper part of the NWs, excluding the topmost part of it. STEM image in Figure 3d shows that the strong-emission segment contains a high-density of stacking faults, with WZ segments and twin defects, while the low-emission part only has a very low density of isolated twins (Figure 3e).

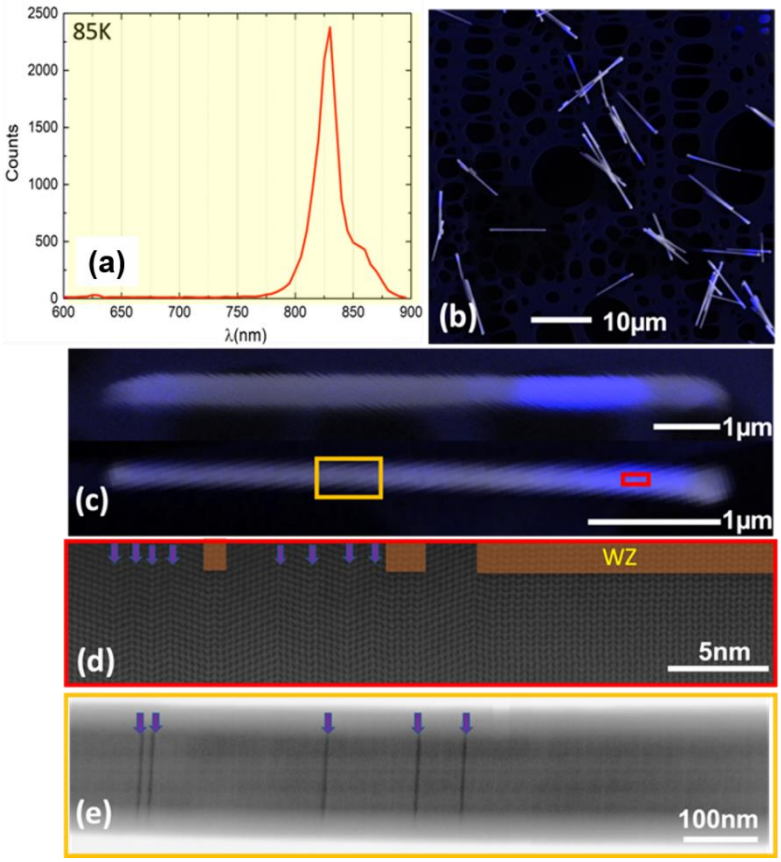

Figure 3. GaAs core-shell NWs with Si-doped shell ($2\times10^{19}cm^{-3}$). (a) CL spectrum of the NW. (b) Panchromatic CL mapping of NWs on a TEM carbon support grid. (c) SEM image (greyscale) with an overlaid panchromatic CL map (blue) of one representative NW. (d) Atomic-resolution bight field (BF) STEM image of the NW segment marked by red square in (c). (e) Low-magnification STEM image of the NW segment marked by yellow square in (c). The twin defects in (d) and (e) are indicated by the blue arrows.

Compared with the middle and lower parts of pure ZB crystalline NWs, the tips of NWs containing additional WZ crystalline phases should contain high-density stacking faults, which in principle leads to stronger emission from the tips. An undoped sample was produced to confirm this. In order to minimize the influence of surface states, we sandwiched a GaAs well with a thickness of 10 nm into a $GaAs_{0.54}P_{0.46}$ barrier (Figure 4a and b) to distinguish the emission characteristics of different GaAs phases. From Figure 4c-e, it can be seen that there

are high-density stacking faults at the NW tip, while the rest are pure ZB with occasional twinning. Contrary to our expectations, the emission at the tip of NWs (approximately 1 μm in length) is much weaker than at other positions, which can be confirmed by the comprehensive CL emission intensity along the NW length shown in Figures 4f and g. In addition, the CL features of multiple NWs shown in Figures 4h and i further confirm that emission is almost undetectable at the tip. In fact, WZ and ZB phases in GaAs NWs have a type-II band alignment, which can lead to low carrier recombination efficiency at the tip of NWs,[47] so it can explain the weaker emission observed in undoped NWs. However, on the contrary, strong emission was observed in the tip region of Si doped NWs. Therefore, the strong emission at the tip of Si doped NWs cannot be simply explained as the better emission efficiency of stacking faults or WZ phases.

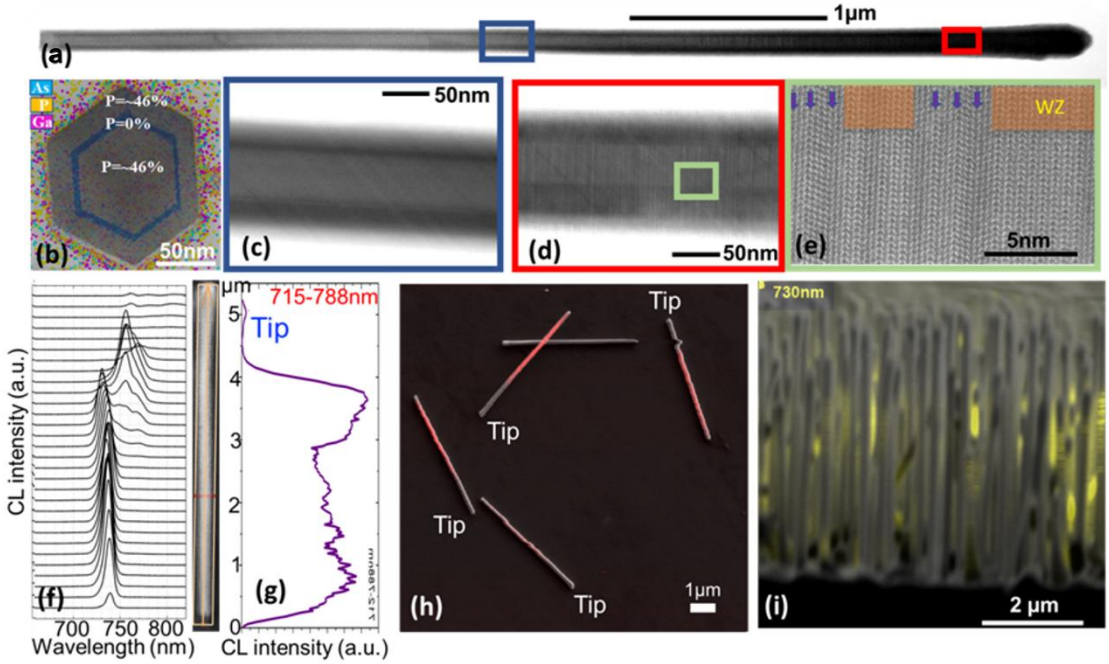

Figure 4. Undoped GaAs(P) core-shell NWs with a GaAs quantum well. (a) Low-magnification STEM image of a representative NW. (b) EDX Compositional mapping of a NW cross section from the <111> region. (c) and (d) Low-magnification STEM images of the

segments marked in (a). (e) Atomic-resolution BF-STEM image of the NW segment marked by the square in (d). The regions marked by the green square have WZ structure and the twin defects are indicated by the blue arrows. (f) CL spectra and (g) integrated CL intensity (715~788 nm) along the axis of the NW shown in between them. (h) Monochromatic CL mapping of several NWs taken at 744 nm under 85 K overlaid with SEM image. The tip of NWs is identified. (i) CL mapping of as-grown NW assemble recorded at 730 nm under the temperature of 8 K.

Apart from the structure, the other major difference between samples in Figure 2 and 4 is the doping. Thus, the Si concentration along the NWs was characterized by Micro-Raman measurement. According to the Pinczuk's model,[48] the increase of doping induces a reduction of the LO/TO ratio in the Raman spectrum. As shown in Figure 5, the LO/TO is much lower for the "tip" point, indicating much higher doping compared with the rest of the NWs. One possibility lead to this doping difference could be the shadowing effect caused by the neighbouring NWs. In our MBE system, the Si effusion cell is angled 33° relative to the substrate normal and the inter-wire distance is in general larger than 2 μm according to Figure 2e. Thus, the shadow from neighbouring NWs can affect the material collection at least 3 μm below the tip of NWs, however, it cannot explain that the bright emission segment is only ~1 μm at the tip shown in Figure 3b and c.

The correlation between the crystal structure and the doping concentration is then investigated by measuring the ratio of E_2/TO that can be considered as proportional to the percentage of WZ crystal phase.[49] According to the presence of an E_2 signal, it can be found that the tip part is much higher in percentage of the WZ phase in Figure 5, which can be observed in all the NWs measured. Meanwhile, the WZ phase percentage of other parts is negligible, which is also in accordance with the TEM measurement mentioned above. As mentioned earlier, the tips of the NWs have a higher Si doping concentration. Therefore, the WZ phase has a higher Si concentration.

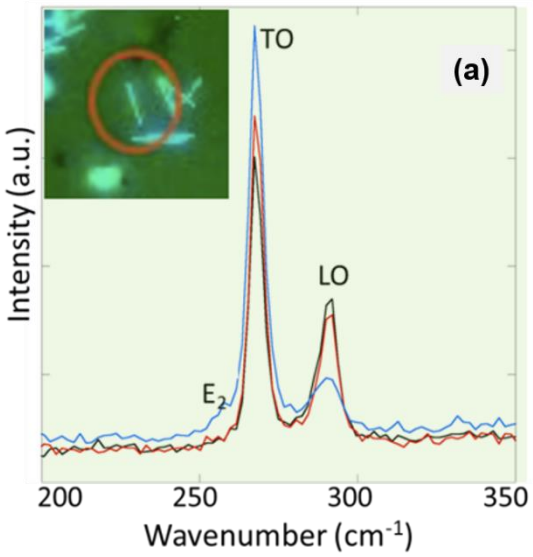

(c)	tip	middle	bottom
LO/TO	0.14	0.38	0.50
Si%	high	low	low
E_2/TO	0.08	0.00	0.00
WZ%	high	low	low

Figure 5. Si doping concentration of core-shell GaAs NWs. (a) Raman spectra from (b) bottom, middle, and tip part of a NW with a nominal doping concentration of 1.3×10^{18} cm^{-3}. The inset is the optical image of the NW used in the measurement. The LO/TO and E_2/TO are listed in the table (c).

The theoretical calculations were performed using plane-wave pseudopotential density functional theory (DFT) to explain this observation. The results show that the Si doping of WZ lead to a dopant formation energy of -0.502 eV/atom, which is more than 2 times lower than that of the doping of ZB (-0.196 eV/atom), as shown in Figure 6. This can explain the higher Si concentration of the NW tip , as the tip has a high percentage of WZ phase. Since the higher Si concentration can generate more free electrons, when the NW does not have an efficient surface passivation, the tips of the NWs with higher Si doping concentration contains more carriers to screen more surface states and reduce the NW depletion.[19,20] Thus, the NW shows stronger emission at the tip. On the other hand, high-density defects commonly generate at the tips of the NWs due to the un-optimized droplet consumption (Figure 2i), and a large percentage of those defects have broken bonds that can act as highly-efficient non-radiative recombination centres.[50] This further explains why the emission from the NW tip is much higher. It needs to be mentioned here that despite the middle and bottom parts of the NW have the similar crystal structure, the shadowing effect can already affect the Si flux collection at this lower height, which caused the slightly lower Si doping concentration at the bottom.

The theoretical calculations also predict that the Si doping of As-sites is not energetically favourable compared to the Ga-sites in both structures.[23] Especially, the As-site doping energy of WZ phases (-0.00109 eV/atom) is 460 times higher compared with that of Ga sites (-0.502 eV/atom), which suggests a much lower doping compensation effect compared with ZB phases. More systematic experimental work will be needed to confirm this prediction in the future. It also needs to be mentioned that the shell doping via Vapor-Solid epitaxial growth (VS) on the NW core may be different from the doping of the NW core itself that grows via the droplet catalysed vapour-liquid-solid (VLS) process. In VS shell growth, it is commonly grown with balanced III-V ratios, which allows the dopants to find their preferred doping sites, while in the VLS growth, it is normally under the super-group-III-rich growth environment in the droplet which can drive the dopants to the group-V sites, despite it is not energetically favourable.[29]

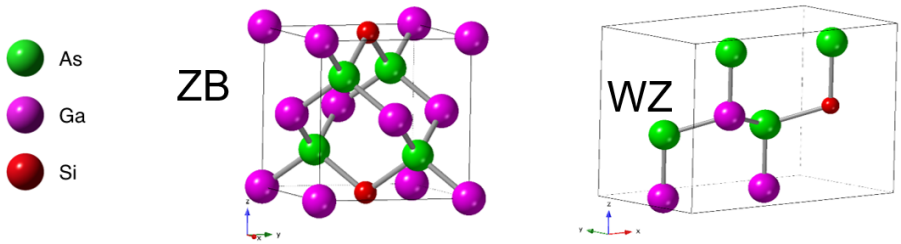

	ZB, Energy / atom, eV	WZ, Energy / atom, eV
Si-Ga	-0.196	-0.502
Si-As	-0.0782	-0.00109

Figure 6. DFT modelling the doping energy of Si into the GaAs of different crystal phases and sites. Images correspond to the doping structure. The doping energies per atom are shown in the image.

Conclusion

In conclusion, the doping behavior differences between WZ and ZB are studied with Si-doped GaAs NW shells. The Si dopant is observed to have a higher incorporation efficiency into WZ structure due to a 2-times lower incorporation energy compared with doping into ZB

structure. The higher doping concentration allows the generation of more electron carriers to screen more surface states and reduce the NW depletion. Thus, the NWs with an un-passivated surface have stronger emission at the tips where they commonly have a high-density of stacking faults, such as WZ segments. Besides, the theoretical analysis predicts that the Si prefers Ga-sites in both structures. Specifically, the As site doping energy of the WZ structure is several orders of magnitude higher than that of the Ga site, allowing for much lower doping compensation effects. These results provide useful information for understanding the doping performance differences between WZ and ZB crystal phases, which can guide the doping control and hence designing crystal-phase devices.

ASSOCIATED CONTENT

Author Information:

Corresponding Author: Yunyan Zhang, yunyanzhang@zju.edu.cn, Hui Yang, h.yang.14@ucl.ac.uk.

ORCID:

Yunyan Zhang: 0000-0002-2196-7291.

Declaration of Competing Interest:

The authors declare no competing financial interest.

Acknowledgements:

The authors acknowledge the support of Leverhulme Trust, EPSRC (grant nos. EP/P000916/1 and EP/P000886/1), and EPSRC National Epitaxy Facility. The authors are grateful to Mr. Marco Guaragno (CNR-ISM) for his technical support with Micro-Raman experiments.

References

(1) Lieber, C. M.; Wang, Z. L. Functional nanowires. *MRS Bull.* **2007**, 32, 99-108.

(2) Zhang, Y.; Wu, J.; Aagesen, M.; Liu, H. III-V Nanowires and Nanowire Optoelectronic Devices. *J. Phys. D: Appl. Phys.* **2015,** 48, 463001.

(3) Yan, R.; Gargas, D.; Yang, P. Nanowire Photonics. *Nat. Photonics* **2009,** 3, 569-576.

(4) Dasgupta, N. P.; Sun, J.; Liu, C.; Brittman, S.; Andrews, S. C.; Lim, J.; Gao, H.; Yan, R.; Yang, P. Semiconductor Nanowires-Synthesis, Characterization, and Applications. *Adv. Mater.* **2014**, 26, 2137-2184.

(5) Yang, P.; Yan, R.; Fardy, M. Semiconductor Nanowire: What's Next?. *Nano lett.* **2010,** 10, 1529-1536.

(6) Yu, X.; Wang, H.; Lu, J., Zhao, J.; Misuraca, J.; Xiong, P. and von Molnár, S. Evidence for Structural Phase Transitions Induced by the Triple Phase Line Shift in Self-catalyzed GaAs Nanowires. *Nano lett.* **2012**, 12, 5436.

(7) Dick, K. A.; Thelander, C.; Samuelson, L.; Caroff, P. Crystal Phase Engineering in Single InAs Nanowires. *Nano lett.* **2010**, 10, 3494.

(8) Tizei, L. H. G.; Amato, M. Electronic Structure and Optical Properties of Semiconductor Nanowires Polytypes. *Eur. Phys. J. B* **2020**, 93, 16.

(9) Assali, S.; Zardo, I.; Plissard, S.; Kriegner, D.; Verheijen, M. A.; Bauer, G.; Meijerink, A.; Belabbes, A.; Bechstedt, F.; Haverkort, J. E.; Bakkers, E. P. Direct Band Gap Wurtzite Gallium Phosphide Nanowires. *Nano lett.* **2013**, 13, 1559-1563.

(10) Fadaly, E. M. T.; Dijkstra, A.; Suckert, J. R.; Ziss, D.; Van Tilburg, M. A. J.; Mao, C.; Ren,Y.;vanLange, V. T.; Korzun, K.; Kölling, S.; Verheijen, M. A.; Busse, D.; Rodl, C.; Furthmuller, J.; Bechstedt, F.; Stangl, J.; Finley, J. J.; Botti, S.; Haverkort, J. E. M.; Bakkers, E. Direct-bandgap Emission from Hexagonal Ge and SiGe Alloys. *Nature* **2020**, 580, 205-209.

(11) Cartoixà, X.; Palummo, M.; Hauge, H. I. T.; Bakkers, E. P. A. M.; Rurali, R. Optical Emission in Hexagonal SiGe Nanowires. *Nano Lett*. **2017**, 17, 4753-4758.

(12) Akopian, N.; Patriarche, G., Liu, L.; Harmand, J. C. and Zwiller, V. Crystal Phase Quantum Dots. *Nano lett.* **2010**, 10, 1198-1201.

(13) Sun, J.; Zhuang, X.; Fan, Y.; Guo, S.; Cheng, Z.; Liu, D.; Yin, Y.; Tian, Y.; Pang, Z.; Wei, Z. and Song, X. Toward Unusual-High Hole Mobility of *p*-Channel Field-Effect-Transistors. *Small*, **2021**, 17, 2102323.

(14) Zhang, Y.; Sanchez, A. M.; Aagesen, M.; Huo, S.; Fonseka, H. A.; Gott, J. A.; Kim, D.; Yu, X.; Chen, X.; Xu, J.; Li, T.; Zeng, H.; Boras, G.; Liu, H. Growth and Fabrication of High-Quality Single Nanowire Devices with Radial p-i-n Junctions. *Small* **2019**, 15, 1803684.

(15) Ra, Y. H.; Lee, C. R. Core-Shell Tunnel Junction Nanowire White-Light-Emitting Diode. *Nano Lett.* **2020**, 20, 4162-4168.

(16) Kim, D. M.; Jeong, Y. H. Nanowire Field Effect Transistors: Principles and Applications; Springer: New York, 2014.

(17) Zeng, X.; Otnes, G.; Heurlin, M.; Mourão, R. T.; Borgström, M. T. InP/GaInP Nanowire Tunnel Diodes. *Nano Res.* **2018**, 11, 2523-2531.

(18) Heurlin, M.; Wickert, P.; Fält, S.; Borgström, M. T.; Deppert, K.; Samuelson, L.; Magnusson, M. H. Axial InP Nanowire Tandem Junction Grown on a Silicon Substrate. *Nano Lett.* **2011**, 11, 2028-2031.

(19) Boland, J. L.; Casadei, A.; Tütüncüoglu, G.; Matteini, F.; Davies, C. L.; Jabeen, F.; Joyce, H. J.; Herz, L. M.; Fontcuberta i Morral, A.; Johnston, M. B. Increased Photoconductivity Lifetime in GaAs Nanowires by Controlled *n*-Type and *p*-Type Doping. *ACS Nano* **2016**, 10, 4219-4227.

(20) Burgess, T.; Saxena, D.; Mokkapati, S.; Li, Z.; Hall, C. R.; Davis, J. A.; Wang, Y.; Smith, L. M.; Fu, L.; Caroff, P.; Tan, H. H.; Jagadish, C. Doping-Enhanced Radiative Efficiency Enables Lasing in Unpassivated GaAs Nanowires. *Nat. Commun.* **2016**, 7, 11927.

(21) Casadei, A.; Krogstrup, P.; Heiss, M.; Röhr, J. A.; Colombo, C.; Ruelle, T.; Upadhyay, S.; Sørensen, C. B.; Nygård, J.; Fontcuberta i Morral, A. Doping Incorporation Paths in Catalyst-Free Be-Doped GaAs Nanowires. *Appl. Phys. Lett.* **2013**, 102, 013117.

(22) Chia, A. C. E.; LaPierre, R. R. Analytical Model of Surface Depletion in GaAs Nanowires. *J. Appl. Phys.* **2012**, 112, 063705.

(23) Dimakis, E.; Ramsteiner, M.; Tahraoui, A.; Riechert, H. and Geelhaar, L. Shell-doping of GaAs Nanowires with Si for *n*-type Conductivity. *Nano Res.*, **2012**, 5, 796-804.

(24) Yazdi, S.; Berg, A.; Borgström, M. T.; Kasama, T., Beleggia, M.; Samuelson, L. and Wagner, J. B. Doping GaP Core-Shell Nanowire pn-Junctions: A Study by Off-Axis Electron Holography. *Small*, **2015**, 11, 2687-2695.

(25) Dillen, D. C.; Kim, K.; Liu, E. S.; Tutuc, E. Radial Modulation Doping in Core-Shell Nanowires. *Nat. Nanotechnol.* **2014**, 9, 116-120.

(26) Casadei, A.; Schwender, J.; Russo-Averchi, E.; Rüffer, D.; Heiss, M.; Alarcó-Lladó, E.; Jabeen, F.; Ramezani, M.; Nielsch, K.; Morral, A. F. i. Electrical Transport in C-Doped GaAs Nanowires: Surface Effects. *Phys. Status Solidi RRL* **2013**, 7, 890-893.

(27) Zhang, Y.; Sun, Z.; Sanchez, A. M.; Ramsteiner, M.; Aagesen, M.; Wu, J.; Kim, D.; Jurczak, P.; Huo, S.; Lauhon, L. J.; Liu, H. Doping of Self-Catalyzed Nanowires under the Influence of Droplets. *Nano Lett.* **2018**, 18, 81-87.

(28) Dufouleur, J.; Colombo, C.; Garma, T.; Ketterer, B.; Uccelli, E.; Nicotra, M.; Fontcuberta i Morral, A. P-Doping Mechanisms in Catalyst-Free Gallium Arsenide Nanowires. *Nano Lett.* **2010**, 10, 1734-1740.

(29) Hijazi, H.; Monier, G.; Gil, E.; Trassoudaine, A.; Bougerol, C.; Leroux, C.; Castellucci, D.; Robert-Goumet, C.; Hoggan, P. E.; André, Y.; Isik Goktas, N.; LaPierre, R. R.; Dubrovskii, V. G. Si Doping of Vapor-Liquid-Solid GaAs Nanowires: *n*-Type or *p*-Type? *Nano Lett.* **2019**, 19, 4498-4504.

(30) Ruhstorfer, D.; Mejia, S.; Ramsteiner, M.; Döblinger, M.; Riedl, H.; Finley, J. J.; Koblmüller, G. Demonstration of *N*-Type Behavior in Catalyst-Free Si-Doped GaAs Nanowires Grown by Molecular Beam Epitaxy. *Appl. Phys. Lett.* **2020**, 116, 052101.

(31) Hilse, M.; Ramsteiner, M.; Breuer, S.; Geelhaar, L.; Riechert, H. Incorporation of the Dopants Si and Be into GaAs Nanowires. *Appl. Phys. Lett.* **2010**, 96, 193104.

(32) Han, N.; Wang, F.; Hou, J. J.; Xiu, F.; Yip, S.; Hui, A. T.; Hung, T.; Ho, J. C. Controllable P-N Switching Behaviors of GaAs Nanowires via an Interface Effect. *ACS Nano* **2012**, 6, 4428-4433.

(33) Dubrovskii, V. G.; Hijazi, H. Effect of Arsenic Depletion on the Silicon Doping of Vapor-Liquid-Solid GaAs Nanowires. *Phys. Status Solidi RRL* **2020**, 14, 2000129.

(34) Galicka, M.; Buczko, R.; Kacman, P. Segregation of Impurities in GaAs and InAs Nanowires. *J. Phys. Chem. C* **2013**, 117, 20361-20370.

(35) Ghaderi, N.; Peressi, M.; Binggeli, N.; Akbarzadeh, H. Structural Properties and Energetics of Intrinsic and Si-Doped GaAs Nanowires: First-Principles Pseudopotential Calculations. *Phys. Rev. B* **2010**, 81, 155311.

(36) Giorgi, G.; Amato, M.; Ossicini, S.; Cartoixà, X.; Canadell, E.; Rurali, R. Doping of III-V Arsenide and Phosphide Wurtzite Semiconductors. *J. Phys. Chem. C* **2020**, 124, 27203-27212.

(37). Zhang, Y.; Sanchez, A. M.; Aagesen, M.; Huo, S.; Fonseka, H. A.; Gott, J. A.; Li, T. Growth and Fabrication of High-Quality Single Nanowire Devices with Radial p-i-n Junctions. *Small*, **2019,** 15, 1803684.

(38) Zhang, Y.; Fonseka, H. A.; Yang, H.; Yu, X.; Jurczak, P.; Huo, S.; Sanchez, A. M.; Liu, H. Thermally-driven Formation Method for Growing (Quantum) Dots on Sidewalls of Self-catalysed Thin Nanowires, Nanoscale Horiz. **2022**, 7, 311.

(39) Kresse, G.; Furthmüller, J. Efficient Iterative Schemes for Ab Initio Total-Energy Calculations Using a Plane-Wave Basis Set. *Phys. Rev. B* **1996**, *54*, 11169-11186.

(40) Perdew, J. P.; Burke, K.; Ernzerhof, M. Generalized Gradient Approximation Made Simple. *Phys. Rev. Lett.* **1996**, 77, 3865.

(41) Liu, B.; Tang, K.; Song, K.; van Aken, P. A.; Yu, Y.; Maier, J.; Song, M. K. and van Aken, P. Electronic supporting information (ESI). *Phys. Rev. B* **1994**, 49, 16223-16233.

(42) Blöchl, P. E. Projector Augmented-Wave Method. *Phys. Rev. B* **1994**, 50, 17953.

(43) Perdew, J. P.; Burke, K.; Ernzerhof, M. Generalized Gradient Approximation Made Simple. *Phys. Rev. Lett.* **1996**, 77, 3865-3868.

(44) Grimme, S.; Ehrlich, S.; Goerigk, L. Effect of the Damping Function in Dispersion Corrected Density Functional Theory. *J. Comput. Chem.* **2011**, 32, 1456-1465.

(45) Zhang, Y.; Aagesen, M.; Holm, J. V.; Jørgensen, H. I.; Wu, J.; Liu, H. Self-Catalyzed GaAsP Nanowires Grown on Silicon Substrates by Solid-Source Molecular Beam Epitaxy. *Nano Lett.* **2013**, 13, 3897-3902.

(46) Wagner, A. R. and Ellis, S. W. Vapor-liquid-solid mechanism of single crystal growth. *Appl. Phys. Lett.* **1964**, 4, 89-90.

(47) Vainorius, N.; Jacobsson, D.; Lehmann, S.; Gustafsson, A.; Dick, K. A.; Samuelson, L.; Pistol, M. E. Observation of Type-II Recombination in Single Wurtzite/Zinc-Blende GaAs Heterojunction Nanowires. *Phys. Rev. B* **2014**, 89, 165423.

(48) Pinczuk, A.; Ballman, A. A.; Nahory, R. E.; Pollack, M. A.; Worlock, J. M. Raman. Scattering Studies of Surface Space Charge Layers and Schottky Barrier Formation in InP. *J. Vac. Sci. Technol.* **1979**, 16, 1168.

(49) Zardo, I.; Yazji, S.; Hormann, N.; Hertenberger, S.; Funk, S.; Mangialardo, S.; Morkotter, S.; Koblmuller, G.; Postorino, P.; Abstreiter, G. E_1(A) Electronic Band Gap in Wurtzite InAs Nanowires Studied by Resonant Raman Scattering, *Nano lett.* **2013**, 13, 3011.

(50) Zhang, Y.; Fonseka, H. A.; Aagesen, M.; Gott, J. A.; Sanchez, A. M.; Wu, J.; Kim, D.; Jurczak, P.; Huo, S.; Liu, H. Growth of Pure Zinc-Blende GaAs(P) Core-Shell Nanowires with Highly Regular Morphology. *Nano Lett.* **2017**, 17, 4946-4950.

Table of Contents